


G.Q. YU
B.K. TAY 
Z.W. ZHAO

Structure and properties of zirconium oxide thin films prepared by filtered cathodic vacuum arc

School of Electrical and Electronic Engineering, Nanyang Technological University, Singapore, 639798, Singapore

Received: 19 September 2003/Accepted: 17 January 2004
Published online: 1 April 2004 • © Springer-Verlag 2004

ABSTRACT Zirconium oxide (ZrO_2) thin films deposited at room temperature by the filtered cathodic vacuum arc (FCVA) technique are detailed in terms of the film structure, composition, morphology, and optical and mechanical properties, which are tailored by the oxygen (O_2) flow rate during deposition. The relationships between the film structure, composition, morphology, and properties are emphasized. With an increasing O_2 flow rate, the film evolves in structure from amorphous, through a pure monoclinic phase with varying preferential orientation, to amorphous again, accompanied by an increase in the O/Zr atomic ratio and a conversion of Zr ions from low oxidation states into Zr^{4+} . Such a structural trend arises from the change in composition, and influences the film morphology and mechanical properties so that the amorphous films exhibit small clusters on the surface and smoother morphology as well as lower hardness compared with the polycrystalline films. The film composition rather than the density dominates the optical properties, where the transmittance and the optical band gap increase with increasing O/Zr values, while the refractive index and extinction coefficients behave conversely with the lowest refractive index (2.16 at 550 nm) approaching the bulk value (2.2).

PACS 68.55.Jk; 78.66.Nk; 68.37.Ps


1 Introduction

Zirconium oxide (ZrO_2) has three temperature dependent polymorphic structures at atmospheric pressure. A monoclinic phase is stable at temperature below 1170 °C, a tetragonal between 1170 and 2370 °C, and a cubic from 2370 °C to the melting point at 2680 °C. ZrO_2 is widely used in optical fields [1–3], because of its high refractive index, large optical band gap, and low optical loss and high transparency in the 0.3–8 μm range. In addition, ZrO_2 is a promising candidate to replace silicon dioxide as the gate dielectric in transistors, due to its high dielectric constant (~ 25), low leakage current level, etc. [4–6]. Furthermore, ZrO_2 has potential as a thermal barrier coating in devices due to its low thermal conductivity [7, 8]. Other properties such as high hardness, large resistance against oxidation, also make it interesting as

a mechanical material [9]. To date, many efforts to prepare ZrO_2 have been made by various deposition techniques, for example, reactive magnetron sputtering [10–13], ion-assisted reactive sputtering or evaporation deposition [8, 14–25], sol-gel methods [26], chemical vapor deposition [4, 17], and so on. The film properties are generally strongly dependent on the deposition process and parameters.

The filtered cathodic vacuum arc technique (FCVA) [27–29], operated at low pressure, low voltage, and high current, effectively eliminates micro-sized (0.1–10 μm) macro-particles from being emitting from cathode materials during arcing by means of mechanical, magnetic, or electrical filters, or a combination of these. It also provides an intense source of fully ionized deposition species with energies (50–150 eV) greater than counterparts produced in thermal evaporation or magnetron sputtering [30, 31]. The removal of detrimental macro-particles undoubtedly improves the resulting film quality and extends the application of the deposition technique. The inherent high-energy could increase the film adhesion and the packing density. The full ionization of the deposition species allows tailoring of the film properties with substrate bias, since kinetic energy is one of the most important parameters as in ion beam assisted deposition (IBAD) [8]. This technique has been demonstrated in the preparation of a diamond-like carbon film with high thermal stability and a high sp^3 [32], to fill trenches [33, 34], as well as the synthesis of certain metal oxide films [35, 36]. However, to the best of our knowledge, little work has been reported on ZrO_2 synthesis by the (FCVA) technique.

In the present work, we systematically investigate the structural, chemical composition, optical, and mechanical properties of ZrO_2 films deposited at different oxygen (O_2) flow rates by FCVA. The emphasis is placed on the relationships between structure, composition, surface morphology, and properties of the films. Our results disclose that the structural and compositional properties of the films are considerably influenced by the O_2 flow rate. The variation in composition induces structural transformation from amorphous through a pure monoclinic phase to amorphous again, and determines the optical properties, whereas the change in structure controls the mechanical properties and affects the surface morphology. The properties of the films are also cross-compared with those of films prepared by other methods to highlight the FCVA features.

 Fax: +65-67/933-318, E-mail: ebktay@ntu.edu.sg

2 Experimental

A schematic diagram of the FCVA deposition system is shown in Fig. 1. The details regarding the main principles of the system have been described elsewhere [37]. Briefly, the system incorporates an off-plane double bend filter, which effectively removes macro-particles originating from the arc itself. A Zr cathode (99.98% pure) operated at 120 A dc current is ignited through instant contact between cathode and anode to obtain the plasma, which is steered out by a toroidal magnetic field fixed at 40 mT to condense on a substrate. The base pressure of the system, evacuated by a rotary pump and a cryo-pump, can reach 4×10^{-6} Torr. O_2 gas (99.99% pure) is led into the region near the Zr target through a copper tube on which many tiny holes are distributed. This way of introducing O_2 is expected to maximize O_2 ionization due to its relatively increased collision with the plasma, possibly promoting a chemical reaction between O_2 and Zr. The O_2 flow rate chosen here is varied from 10 to 98 sccm corresponding to 1×10^{-4} to 4.6×10^{-4} Torr. During deposition, the deposition rate decreases from 75 to 35 nm/min with an increasing O_2 flow rate as a result of increased oxidation of the target, and collision-induced loss of condensing particles. The films are grown on *n*-Si (100) and quartz substrates at room temperature. All the substrates are sequentially cleaned in acetone, alcohol, and de-ionized water prior to being loaded into the deposition chamber. All the films being investigated are generally around 200 nm thick.

The film phase and crystal structure are identified by X-ray diffraction (XRD) with a $Cu K\alpha$ source at 1.54 \AA . Transmittance and reflectance are recorded from 200 to 1100 nm with a spectrometer. Optical constants are obtained by fitting optical spectra with Scout software [38]. Core level spectra

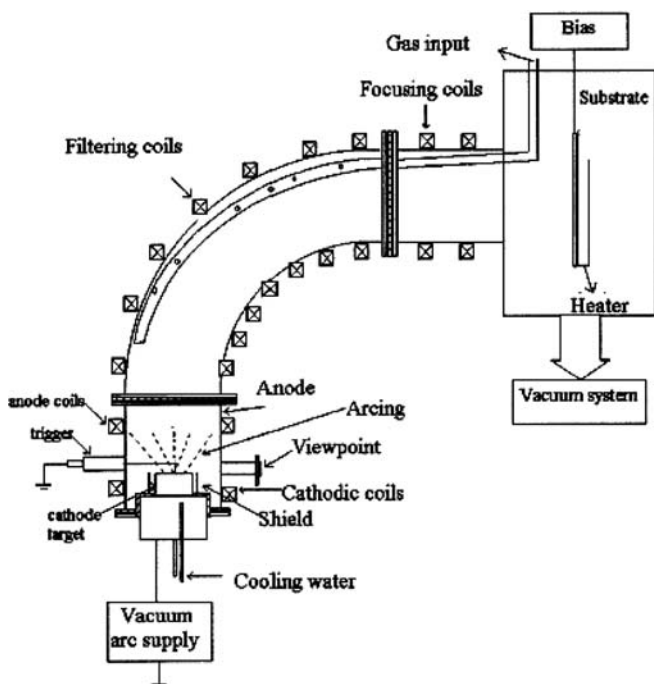


FIGURE 1 A schematic diagram of the FCVA deposition system

and compositional analysis are carried out by X-ray photoelectron spectroscopy (XPS) with monochromatic $Al K\alpha$ radiation (1486.6 eV). No sputter cleaning of the samples is performed to avoid changes in chemical compositions induced by preferential sputtering. The spectrum obtained is corrected by an adventitious $C1s$ peak at 284.6 eV. Surface morphology is measured by atomic force microscopy (AFM) in tapping mode (Dimension 3000 scanning probe microscope from Digital Instruments). The mechanical properties on a nano-scale are obtained by a nanoindentation technique apparatus (Hysitron Inc.) attached to the above AFM equipment. Nanoindentations were made using a Berkovich diamond indenter and the maximum loads applied were 500 μN . The indenter was loaded at 100 $\mu N/s$, held at peak load for 5 s and then finally unloaded at 100 $\mu N/s$.

3 Results

3.1 Structure

Figure 2 shows the XRD patterns for ZrO_2 films deposited at different O_2 flow rates. At 10 sccm, a broad but symmetric peak centered at around 32.4° is observed in curve (a), indicative of an amorphous structure. The peak is believed to come from an oxygen-deficient Zr-O solid solution [40]. Wong et al. [13] also reported a similar phenomenon, where, however, the peak was unsymmetric and sharp. As the O_2 flow rate increases to 20 sccm (Fig. 2b), one peak at 33.7° assigned to (200) planes of monoclinic phase (denoted as $m(200)$) is predominant, accompanied by the appearance of other weak peaks also from the monoclinic phase. This rapid occurring of diffraction peaks shows that so much oxygen is incorporated that sufficient ZrO_2 crystallite forms which can be detected. The easy combination between Zr and O is possibly related to charged and therefore active emitted species, as well as further stimulated by energetic Zr particles bombarding the surface as in IBAD. At 35 sccm, in addition to more weak peaks, the $m(200)$ peak becomes weaker while the $m(-202)$ peak gets stronger. When the O_2 flow rate goes up to 50 sccm, the dominant peak is changed to $m(-111)$ while many more monoclinic peaks are produced. However, when

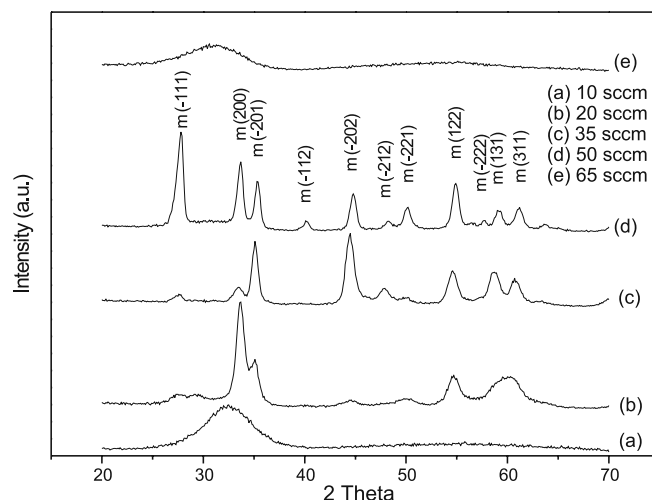


FIGURE 2 XRD patterns for ZrO_2 films deposited at different O_2 flow rate

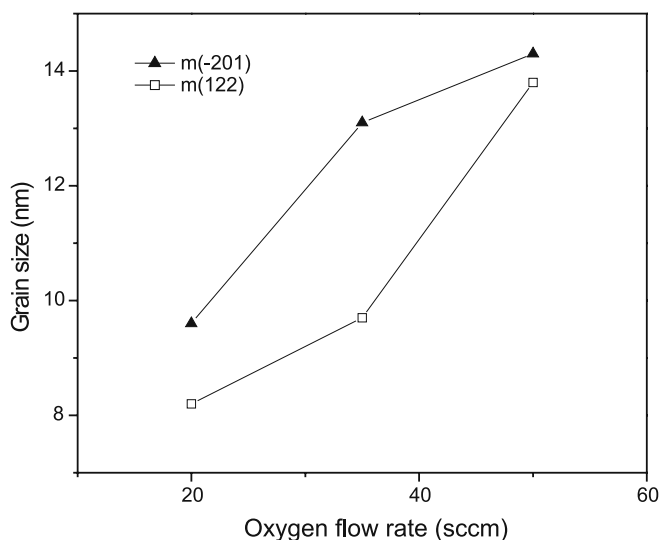


FIGURE 3 Crystallite size of ZrO_2 film at different O_2 flow rates

the O_2 flow rate rises to 65 sccm or above, the film transforms from a polycrystalline into an amorphous structure, evidenced by a broad peak at 31.3° in curve (e). The variation in structure denotes that the O_2 flow rate plays an important role in the structural evolution. In a certain flow rate range (20 to 50 sccm) the films obtained are polycrystalline but in purely monoclinic phase with varying preferred orientation.

Further, Fig. 3 presents the average grain size, D , which is quantified by the Scherrer equation [41],

$$D = (0.9\lambda) / (B \cos \theta), \quad (1)$$

where B is the full width at half maximum (FWHM) in 2θ units, λ is the X-ray wavelength, and θ is the Bragg diffraction angle. Note that the formula does not involve peak broadening arising from stress and defects in the film as well as from instrument itself. Consequently, the grain size calculated from the formula is smaller than the actual value. Even so, a tendency of the crystallite size with O_2 flow rate should not be affected. As displayed, the size increases with increasing O_2 flow rate. Generally, growth of large crystallites is linked with high surface mobility of adatoms [39]. This is verified by Gao et al. [11], who found that the crystallite size of ZrO_2 films deposited by magnetron sputtering increases with decreasing O_2 pressure, which in turn promotes surface mobility of the adatoms. Kao et al. [8] investigated ZrO_2 films prepared by low energy (100 eV) ion assisted reactive deposition, and found that the grain size increases with decreasing energy of the sputtering ion beam. They attributed it to the reduced deposition rate induced by the lower energy of the sputtering ion beam [8]. In our case, the deposition rate also decreases when the O_2 flow rate increases, as mentioned before. Such a reduction leads to a relative lack of condensing species and possibly affects the film nucleation and crystallite growth. The size trend does not veto the general viewpoint. Instead, this implies that for FCVA deposition, condensing species possess enough surface mobility in the flow rate range studied, so that other factors like deposition rate could be dominant enough to affect the crystallite size. That condensing species have enough mo-

bility can be supported by the AFM analysis detailed as follows.

3.2 Chemical compositions and chemical states

It was concluded from a typical XPS survey spectrum (not shown) that besides the peaks contributed by photoelectrons and Auger transitions of Zr and O, C 1s is observed as well, which is mainly from surface contamination after exposure of the sample to air. The two strong peaks at 185.9 and 533.2 eV are identified as Zr 3d and O 1s, respectively. Fig. 4 presents the normalized Zr 3d (a) and O 1s (b) XPS local spectra for the film prepared at 50 sccm. The spectra closely resemble those observed in standard monoclinic ZrO_2 [42]. Two peaks, Zr $3d_{5/2}$ and Zr $3d_{3/2}$ observed at binding energies of 181.8 and 184.2 eV, very near to the values of Zr^{4+} in ZrO_2 [42], are symmetrical, denoting that only one oxidation state of Zr exists in the film. Their intensity ratio ($I_{3d_{5/2}}/I_{3d_{3/2}}$) and energy interval ($\Delta 3d_{5/2}-3d_{3/2}$) resulting from spin-orbit splitting are 1.5 and 2.4 eV, in agreement with other studies [20, 42]. An asymmetric O 1s peak can be decomposed into two components peaked at a low binding energy (LBE) of 529.6 eV and high binding energy (HBE) of 531.6 eV, quite comparable with reported ones [14, 43]. It has been accepted that the LBE peak is assigned to the oxygen in zirconia [14, 20, 43] while the HBE is attributed to oxygen present in the hydroxide and/or adsorbed oxygen or carbonates or higher-valent oxides [14, 42, 44, 45]. Matsuo et al. [20] ascribed it to oxygen possibly bound to Zr.

In contrast, for the film deposited at the low flow rate, i.e., 35 sccm, the Zr 3d spectrum is somehow different whereas the O 1s spectrum is very similar. A shoulder of the Zr $3d_{5/2}$ clearly appears at the lower binding energy side (Fig. 4c), indicating that other oxidation states of Zr (Zr^{n+} , $n = 1, 2, 3$) occur. This shoulder is attributed to Zr suboxides [14, 20]. It can be concluded from this discrepancy that with increasing flow rate, Zr^{n+} ($n \leq 3$) will convert into Zr^{4+} due to a full reaction between O and Zr in the films. This consistent variation in the oxidation state of Zr ions with the film composition was also reported in [20]. The atomic ratio of O to Zr (O/Zr) in the films can be calculated with their respective peak areas cali-

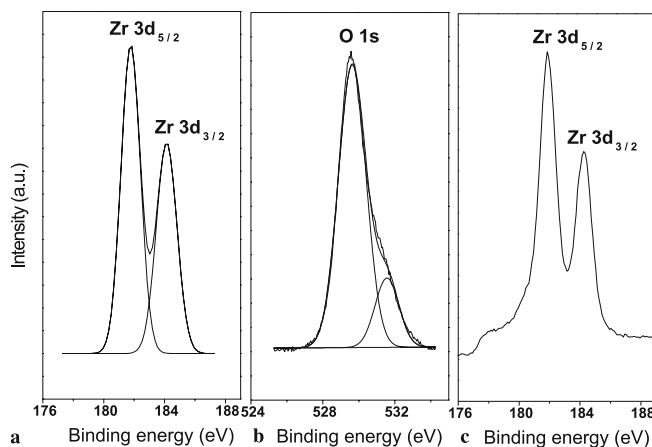


FIGURE 4 Zr 3d a, and O 1s b, XPS local spectra of the film deposited at 50 sccm and Zr 3d c, at 35 sccm

brated by their sensitivity factors (0.66, 2.1, 0.66 for O 1s and Zr 3d). For the calculation, the O 1s HBE peak is not included due to its small fraction. As expected, the O/Zr ratio increases with more addition of oxygen (not shown). Note that for the film deposited at 50 sccm, the O/Zr ratio obtained is approximately 1.98 : 1, near to the ideal stoichiometric ratio of 2 : 1. At 65 sccm and above, the films are over-stoichiometric ($\sim 2.2 : 1$).

3.3 Surface morphology

Figure 5a presents a typical top-view AFM image of the film at 65 sccm. On the film surface, the clusters composed of many condensing adatoms are uniformly distributed. The surface is quite clear and smooth, with its root-mean-square (RMS) roughness less than 0.1 nm over the area of $1 \mu\text{m} \times 1 \mu\text{m}$. This clearness and smoothness is associated with the above-mentioned high energy of bombarding particles, which possibly removes loose particles (so-called

“self-sputtering”) or promotes bonding between adatoms and offers the adatoms enough lateral mobility on the growing surface [39, 46], again suggesting that the flow rate range selected does not greatly affect the adatoms mobility, in accordance with the XRD results.

Interestingly, the film morphology seems to be affected by the O_2 flow rate as well. At 10 sccm, the clusters distributed on the film surface are similar in size to that for the film at 65 sccm. However, in the range of 20 to 50 sccm, larger clusters are present on the surface. This change in cluster size is also reflected in the curve of roughness versus the O_2 flow rate (Fig. 5b), where the roughness is larger for a 20–50 sccm flow rate range. The flow rate-dependent surface morphology could be correlated with the film structural change as drawn from XRD analysis. In other words, compared with the amorphous films, the polycrystalline films formed in a 20–50 sccm flow exhibit larger clusters on the surface and look relatively rougher.

3.4 Optical properties

Figure 6 displays the transmittance spectra of the films prepared at different O_2 flow rates on quartz as well as on uncoated substrates. The O_2 flow rate is found to have a high influence on film transmittance. At 10 sccm, the film appears dark and the transmittance almost goes to zero. When the O_2 flow rate increases to 20 sccm, the transmittance is slightly enhanced, especially in the long wavelength range. The low transmittance may result from light absorption by free carriers from Zr, most of which would not yet be oxidized. Further increasing to 35 sccm leads to a great improvement in the transmittance, although the film is not fully transparent. The largely increased transmittance at 35 sccm suggests that most of the Zr in the film has bonded to O due to more incorporation of oxygen, agreeing with the XPS results. When the O_2 flow rate is at 50 sccm and above, an interference pattern is clearly seen indicating that the films are transparent, and a better transmittance can be achieved. The maximum transmittance is close to that of the bare substrate (curve (e)),

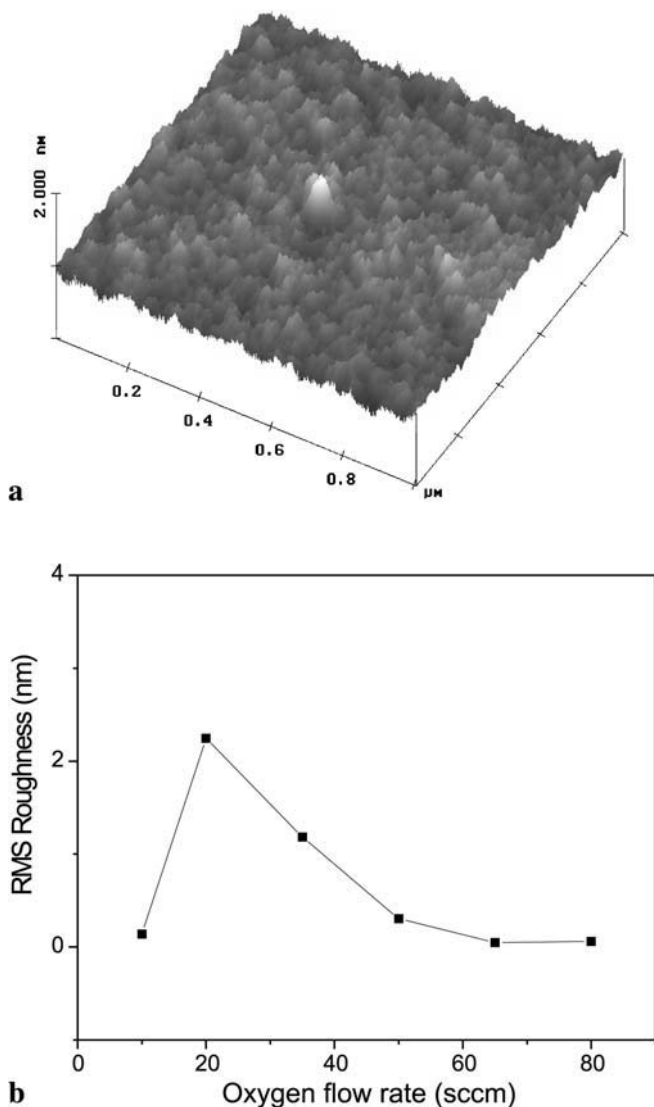


FIGURE 5 a A top-view AFM image of the film at 65 sccm; b The RMS roughness of the films at varying O_2 flow rates

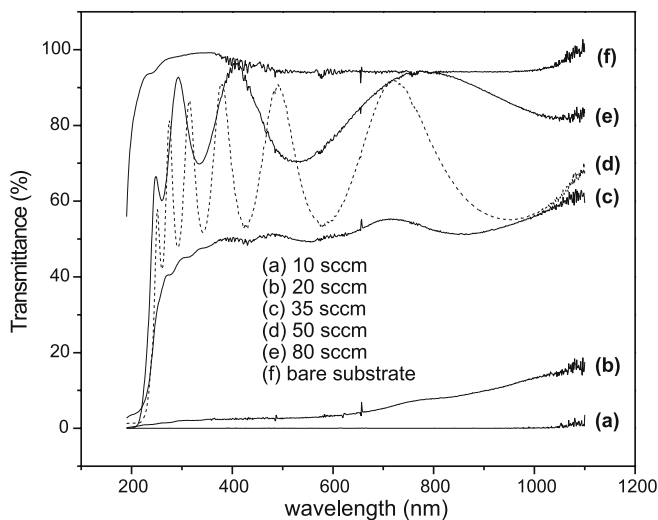


FIGURE 6 Transmittance spectra of the films prepared at different O_2 flow rate

indicating that the film has approached an ideal stoichiometry (2 : 1) in terms of the O/Zr ratio, as shown by XPS analysis. Also, a blue shift in the absorption edge (less than 400 nm) is observed with increasing O₂ flow rate, implying enlargement in the optical band gap with more oxygen incorporation into the film, as discussed next.

The optical band-gap energy, E_g , of the film can be determined from the Tauc equation [47],

$$\alpha h\nu = \beta(h\nu - E_g)^2, \quad (2)$$

where α is an absorption coefficient, $h\nu$ the energy of incident light quanta, and β a constant. The optical band gap is given in Fig. 7 as a function of the O₂ flow rate, where the band gaps at 10 and 20 sccm cannot be acquired by this method due to high absorption. Insets are the plots of $(\alpha h\nu)^{1/2}$ and absorption coefficient versus $h\nu$, respectively. As observed, the optical band gap energy first increases with increasing flow rate, from 4.1 eV at 35 sccm to 5.0 eV at 50 sccm, and then saturates at 5.0 eV, within the range reported (3.25 ~ 5.1 eV) [48]. A drastic increment in absorption beyond the band gap is observed due to the band–band transitions [49, 50].

Figure 8 shows the variation of optical constants at 550 nm with the O₂ flow rate. The refractive index monotonously decreases with increasing flow rate. Following results from published reports [8, 10, 14, 17, 18], the refractive index is possibly correlated with the structure, chemical composition, and packing density of film. As concluded, the film evolves in structure from amorphous to monoclinic phase with increasing flow rate to 50 sccm at which the film is of ideal stoichiometry, and then to amorphous at above 50 sccm at which the film is over-stoichiometry. The inconsistent dependence of the index and structure on flow rate denotes that the structure is not a significant factor to determine the index. In addition, the film density is believed to decrease with increasing flow rate and to contribute to a decrease of the index. However, as depicted below, the degree of reduction in density is not severe. This is substantiated by the fact that the index (2.16) at 80 sccm

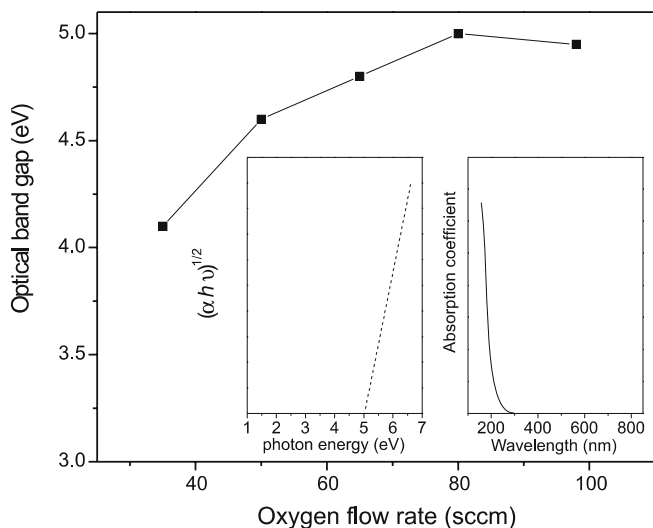


FIGURE 7 The optical band gap of the films with varying O₂ flow rate

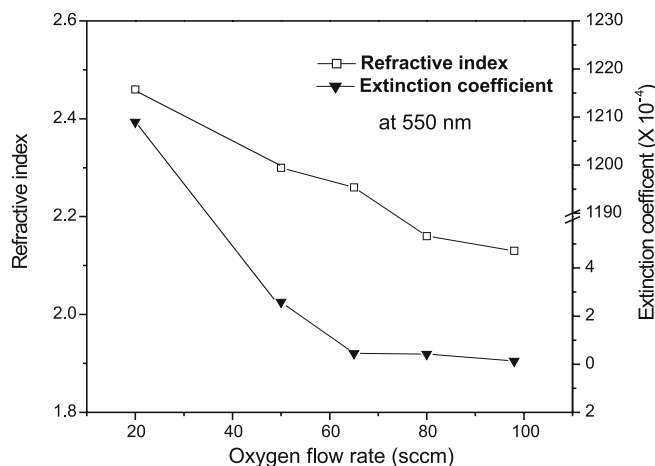


FIGURE 8 Refractive index and extinction coefficient of the films at various O₂ flow rates

is very near the bulk value of 2.2 [51], and higher than those prepared by other techniques [8, 10–12, 14, 16–18, 24]. Therefore, we conclude that the composition is a dominant factor affecting the index. Kao et al. also reported a similar conclusion [8].

The extinction coefficient decreases to approximately zero with increasing flow rate. This is consistent with the trend of the refractive index and hence is associated with a reduction of oxygen vacancies in the films caused by more incorporation of oxygen. Especially at 50 sccm, the film exhibits a sharp drop in the extinction coefficient, denoting O/Zr an atomic ratio approaching 2 : 1, as confirmed by XPS. The increment in crystallite size is also another cause to decrease extinction coefficient [11]. When the crystallite size becomes greater, scattering center concentration related to grain boundary in the film correspondingly decreases, which results in less light loss. Considering that the crystallite size is not changed much in our case, we believe it is not a significant contributing factor.

3.5 Mechanical properties

The film hardness is a measure of resistance to plastic deformation and defined as the peak load divided by the corresponding indentation area. Practically, the hardness is obtained by fitting the unloading data with a power law equation [39]. The mechanical properties of the films as a function of flow rate are displayed in Fig. 9, where the values are averaged at least three times. Both the microhardness and Young's modulus are apparently dependent upon the O₂ flow rate. When flow rate increases from 10 to 20 sccm, the hardness almost stays at about 13.6 GPa. Further increasing the flow rate leads to an abrupt increase in hardness. At 35 and 50 sccm, the increase is pronounced. However, beyond 50 sccm, the film starts to become soft and at 65 sccm drops to 13.4 GPa in hardness. Clearly, the change in hardness is very similar to the structural variation observed in the XRD patterns. This signifies that the film structure rather than the composition determines the film hardness, which is not in agreement with the result reported by Kao [19].

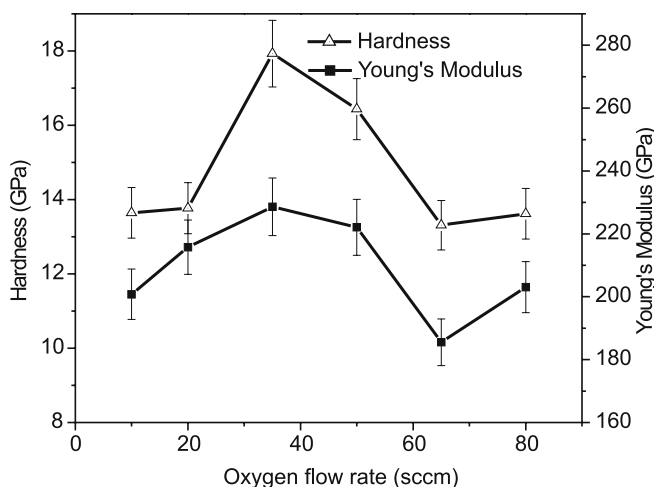


FIGURE 9 The film hardness and Young's modulus at different O_2 flow rates

4 Discussion

The above results have shown that the film structure, composition, morphology, optical, and mechanical properties are all affected by the O_2 flow rate. Increasing the O_2 flow rate produces two main effects as follows.

1. The film composition ratio, O/Zr , is increased due to incorporation of more oxygen into them. This results in that the film develops from the Zr metallic phase, through an oxygen-deficient Zr–O solid solution, to zirconium oxide with stoichiometric (2:1 of O/Zr) at 50 sccm or with over-stoichiometric ratio (2.2:1) above 50 sccm, as evidenced from the XRD and XPS results. This over-stoichiometry could be explained by so-called “recoil implantation” [55], in which light elements will be knocked into deeper regions of the sample which is irradiated by energetic particles. As the O_2 flow rate increases, more oxygen is physically or chemically absorbed on the growing surface so that more will be knocked by energetic Zr ions into the growing surface. Due to that O atoms are incorporated into polycrystalline ZrO_2 , Zr ionic radii are changed correspondingly, inducing the change in lattice parameter. With more incorporation, the crystal structure or symmetry is broken. As a consequence, the film structure transforms from polycrystalline at 50 sccm to amorphous at flow rates higher than 50 sccm, as revealed by XRD analysis. The structural change with this composition has been reported in [21]. Details regarding the phase transition are beyond the scope of this work. The compositional variation sharply influences the optical properties of the films, i.e., the transmittance and optical band gap increase with increasing O/Zr values while the refractive index and extinction coefficients decrease with increasing O/Zr value.
2. The associated process pressure is increased. This generally decreases the kinetic energy of condensing Zr species due to increased collisions [54] between Zr and oxygen besides other collision-enhanced effects such as charge transfer, formation of Zr–O, and weakening of the arc plasma density. The kinetic energy of condensing species is well known to be one important parameter in influencing the microstructure and properties of the film. Yushkov

et al. [30, 52, 53] have investigated the dependence of ion energy on deposition conditions in the case of arc deposition. As reported, the kinetic energy of Zr ions from an arcing Zr cathode is about 116 eV and the dependence is valid for pressures up to about 10^{-4} Torr. As the depositions were carried out on floating substrates as in our experiments, a sheath voltage is formed between substrate and plasma, and measured to be about 10–15 eV. The Zr ions therefore acquire a total energy of 126–131 eV upon condensing on substrates. In the present work, the process pressure is varied from 1×10^{-4} to 4.6×10^{-4} Torr with the O_2 flow rate varied from 10 to 98 sccm. Within this small pressure range, the energy of Zr ions, we suppose, is not reduced so much that the condensing species possess enough to effect their migration ability on the growing surface. This assumption can be supported by two facts. One is that the surface roughness of all the films is very low. In general, the surface roughness is closely related to the surface mobility of depositing species. The second is that the lowest refractive index (2.16) of the film at 80 sccm is near the bulk value (2.20). As pointed out above, the refractive index is mainly decided by the film packing density. The denser the film packing density, the larger the refractive index. According to structure zone models [56, 57], the film packing density is largely determined by the adatom mobility, which is affected by the kinetic energy of depositing species and the growth temperature. Increased working pressures cause the coating structure to vary from a dense fibrous form to a voided structure of isolated columnar crystallites. The formation of open structures at elevated working pressures can be suppressed by relatively low energy ion bombardment as in IBAD. In our case, no additional heating of substrates is applied. The rise in the deposition temperature caused by plasma bombardment during deposition is small (around 80 °C). For this reason, the adatom mobility contributed by the deposition temperature is negligible at different flow rates. Therefore, the adatom mobility is dominated by the kinetic energy of Zr species. That all the films possess a dense packing density can be further verified by comparing the transmittance spectra of the films before and after exposure to air for

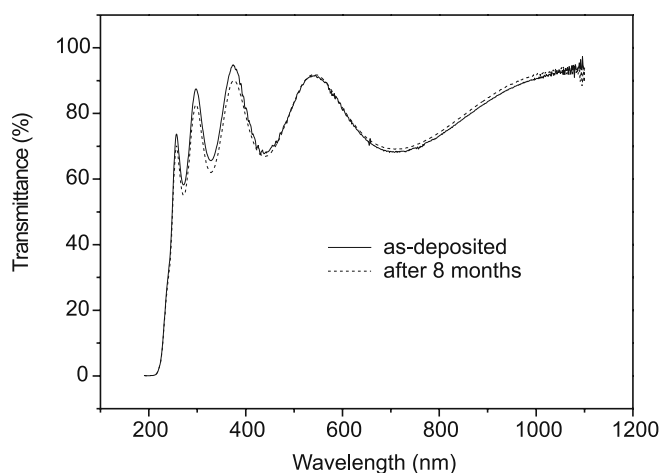


FIGURE 10 Transmittance spectra of the as-deposited film before and after exposure to air for 8 months

8 months as shown in Fig. 10, where little change (shift in peak position or reduction in peak intensity) is observed. This means that the films are so dense that penetration of water vapor into them is negligible. This is also why we believe that a change in film packing density is not mainly responsible for the change of the optical constants with the O_2 flow rate.

5 Conclusions

The structure, composition, morphology, optical, and mechanical properties of ZrO_2 films deposited by the filtered cathodic vacuum arc (FCVA) technique have been investigated at varying O_2 flow rates, up to 98 sccm. The O_2 flow rate is found to be an important parameter in controlling the film structure, composition, and properties. With increasing O_2 flow rate, ZrO_2 film evolves in structure from amorphous, through to a pure monoclinic phase with varying preferential orientation, to amorphous again, concurrent with an increase in the O/Zr atomic ratio, and a conversion of Zr ions from low oxidation states into Zr^{4+} . Such a trend in the structure with the O_2 flow rate is a result of a change in the film composition, and determines the surface morphology and the mechanical properties of the film. The film composition instead of the film density, dominates the optical properties, where transmittance and optical band gap increase with increasing O/Zr value, whereas the refractive index and extinction coefficients behave inversely.

REFERENCES

- 1 T. Koch, P. Ziemann: *Thin Solid Films* **303**, 122 (1997)
- 2 W.H. Loder milk, D. Milam, F. Rainer: *Thin Solid Films* **73**, 155 (1980)
- 3 P.J. Martin, H.A. Macleod, R.P. Netterfield, C.G. Pacey, W.G. Saintry: *Appl. Opt.* **22**, 178 (1983)
- 4 B.O. Cho, J.P. Chang, J.H. Min, S.H. Moon, Y.W. Kim: *J. Appl. Phys.* **93**, 745 (2003)
- 5 G.D. Wilk, R.M. Wallace, J.M. Anthony: *J. Appl. Phys.* **89**, 5243 (2001)
- 6 M. Copel, M. Gribelyuk, E. Gusev: *Appl. Phys. Lett.* **76**, 436 (2000)
- 7 K.C. Fancey, A. Matthews: *J. Vac. Sci. Technol. A* **4**, 2656 (1986)
- 8 A.S. Kao, G.L. Gorman: *J. Appl. Phys.* **67**, 3826 (1990)
- 9 F. Jones: *J. Vac. Sci. Technol. A* **6**, 3088 (1988)
- 10 S. Venkataraj, O. Kappertz, H. Weis, R. Drese, R. Jayavel, M. Wuttig: *J. Appl. Phys.* **92**, 3599 (2002)
- 11 P. Gao, L.J. Meng, M.P. dos Santos, V. Teixeira, M. Andritschky: *Appl. Surf. Sci.* **173**, 84 (2001)
- 12 M.H. Suhail, G. Mohan Rao, S. Mohan: *J. Vac. Sci. Technol. A* **9**, 2675 (1991)
- 13 M.S. Wong, W.J. Chia, P. Yashar, J.M. Schneider, W.D. Sproul, S.A. Barnett: *Surf. Coat. Technol.* **86–87**, 381 (1996)
- 14 E.E. Khawaja, F. Bouamrane, A.B. Hallak, M.A. Daous, M.A. Salim: *J. Vac. Sci. Technol. A* **11**, 580 (1993)
- 15 R. Rujkorakarn, J.R. Sites: *J. Vac. Sci. Technol. A* **4**, 568 (1986)
- 16 P.J. Martin, R.P. Netterfield, W.G. Saintry, C.G. Pacey: *J. Vac. Sci. Technol. A* **2**, 341 (1984)
- 17 M.G. Krishna, K.N. Rao, S. Mohan: *Appl. Phys. Lett.* **57**, 557 (1990)
- 18 M. Bellotto, A. Caridi, E. Cereda, G. Gabetta, M. Scagliotti, G.M. Braga Marcazzan: *Appl. Phys. Lett.* **63**, 2056 (1993)
- 19 A.S. Kao: *J. Appl. Phys.* **69**, 3309 (1991)
- 20 M. Matsuoka, S. Isotani, S. Miyake, Y. Setsuhara, K. Ogata, N. Kuratani: *J. Appl. Phys.* **80**, 1177 (1996)
- 21 M. Matsuoka, S. Isotani, J.F.D. Chubaci, S. Miyake, Y. Setsuhara, K. Ogata, N. Kuratani: *J. Appl. Phys.* **88**, 3773 (2000)
- 22 M. Morita, H. Fukumoto, T. Imura, Y. Osaka, M. Ichihara: *J. Appl. Phys.* **58**, 2407 (1985)
- 23 P.J. Martin, R.P. Netterfield, W.G. Saintry, G.J. Clark, W.A. Lanford, S.H. Sie: *Appl. Phys. Lett.* **43**, 711 (1983)
- 24 P.J. Martin, R.P. Netterfield, W.G. Saintry: *J. Appl. Phys.* **55**, 235 (1984)
- 25 X.L. Jiang, N. Xu: *J. Appl. Phys.* **66**, 5594 (1989)
- 26 E. De la Rosa-Cruz, L.A. Diaz-Torres, P. Salas, D. Mendoza, J.M. Hernandez, V.M. Castano: *Opt. Mat.* **19**, 195 (2002)
- 27 I.G. Brown: *Annu. Rev. Mater. Sci.* **28**, 243 (1998)
- 28 P.J. Martin, A. Bendavid: *Thin Solid Films* **394**, 1 (2001)
- 29 R.L. Boxman, V. Zhitomirsky, B. Alterkop, E. Gidalevich, I. Beilis, M. Keidar, S. Goldsmith: *Surf. Coat. Technol.* **86–87**, 243 (1996)
- 30 G.Y. Yushkov, A. Anders, E.M. Oks, I.G. Brown: *J. Appl. Phys.* **88**, 5618 (2000)
- 31 R.L. Boxman, P.J. Martin, D. Sanders (Eds.), *Handbook of Vacuum Arc Science and Technology*, (Noyes, NY, 1996)
- 32 S. Anders, J. Díaz, J.W. Ager III, R. Yu Lo, D.B. Bogy: *Appl. Phys. Lett.* **71**, 3367 (1997)
- 33 O.R. Monteiro: *J. Vac. Sci. Technol. B* **17**, 1094 (1999)
- 34 G.Q. Yu, B.K. Tay, S.P. Lau, K. Prasad, J.X. Gao: *J. Phys. D: Appl. Phys.* **36**, 1355 (2003)
- 35 Z.W. Zhao, B.K. Tay, D. Sheeja: *Surf. Coat. Technol.* **167**, 234 (2003)
- 36 Z.W. Zhao, B.K. Tay, S.P. Lau, C.Y. Xiao: *J. Vac. Sci. Technol. A* **21**, 906 (2003)
- 37 X. Shi, B.K. Tay, S.P. Lau: *Int. J. Mod. Phys. B* **14**, 136 (2000)
- 38 W. Theiss: In: *Scout Thin Film Analysis Software Handbook*, (Hard- and Software, Aachen, Germany), www.mtheiss.com
- 39 G.Q. Yu, B.K. Tay, S.P. Lau, K. Prasad, L.K. Pan, J.W. Chai, D. Lai: *Chem. Phys. Lett.* **373**, 264 (2003)
- 40 G.P. Abriata, J. Garces, R. Versaci: *Bull. Alloy Phase Diag.* **7**, 116 (1986)
- 41 B.D. Cullity: *Elements of X-ray Diffraction* (2nd ed., Addison Wesley, Reading, MA 1978) p. 102
- 42 T.L. Barr: In: *Quantitative Surface Analysis of Materials*, ed. by N.S. McIntyre (Amer. Soc. for Testing Materials, Philadelphia, 1978) p. 83
- 43 D. Majumdar, D. Chatterjee: *J. Appl. Phys.* **70**, 988 (1991)
- 44 T.L. Barr: *J. Vac. Sci. Technol.* **14**, 660 (1977)
- 45 C. Morant, J.M. Sanz, L. Galan, L. Soriano, F. Rueda: *Surf. Sci.* **218**, 331 (1989)
- 46 X. Wang, X.H. Liu, S.C. Zou, P.J. Martin, A. Bendavid: *J. Appl. Phys.* **80**, 2658 (1996)
- 47 J. Tauc: In: F. Abeles (Ed.) *Optical Properties of Solids* (North-Holland, Amsterdam 1971), p. 71
- 48 J.G. Bendoraitis, R.E. Salomon: *J. Phys. Chem.* **69**, 3666 (1965)
- 49 I. Kosacki, V. Petrovsky, H.U. Anderson: *Appl. Phys. Lett.* **74**, 341 (1999)
- 50 N. Nicoloso, A. Löbert, B. Leibold: *Sens. Actuators B* **8**, 253 (1992)
- 51 M. Ghanashyam Krishna, K. Narasimha Rao, S. Mohan: *Thin Solid Films* **207**, 248 (1992)
- 52 P. Sigmud: *J. Appl. Phys.* **50**, 7261 (1979)
- 53 K. Meyer, I.K. Schuller, C.M. Falco: *J. Appl. Phys.* **52**, 5803 (1981)
- 54 A. Anders, G.Y. Yushkov: *J. Appl. Phys.* **91**, 4824 (2002)
- 55 M.M.M. Bilek, P.J. Martin, D.R. McKenzie: *J. Appl. Phys.* **83**, 2965 (1998)
- 56 R. Messier, A.P. Giri, R.A. Roy: *J. Vac. Sci. Technol. A* **2**, 500 (1984)
- 57 J.A. Thornton: *J. Vac. Sci. Technol. A* **4**, 3059 (1986)